Journal of Physics D: Applied Physics

PAPER

Broad-band photoluminescence of donor–acceptor pairs in tetrahedrite $Cu_{10}Cd_2Sb_4S_{13}$ microcrystals

To cite this article: Jüri Krustok *et al* 2021 *J. Phys. D: Appl. Phys.* **54** 105102

IOP Publishing Journal of Physics D: Applied Physics
J. Phys. D: Appl. Phys. **54** (2021) 105102 (7pp) https://doi.org/10.1088/1361-6463/abce29

Broad-band photoluminescence of donor–acceptor pairs in tetrahedrite $Cu_{10}Cd_2Sb_4S_{13}$ microcrystals

Jüri Krustok[1,2], Taavi Raadik[2], Reelika Kaupmees[2], Fairouz Ghisani[2], Kristi Timmo[2], Mare Altosaar[2], Valdek Mikli[2] and Maarja Grossberg[2]

[1] Division of Physics, Tallinn University of Technology, Ehitajate Tee 5, Tallinn 19086, Estonia
[2] Department of Materials and Environmental Technology, Tallinn University of Technology, Ehitajate Tee 5, Tallinn 19086, Estonia

E-mail: Juri.Krustok@ttu.ee

Received 7 October 2020, revised 9 November 2020
Accepted for publication 26 November 2020
Published 22 December 2020

Abstract

We present temperature and laser power dependent photoluminescence (PL) study of Cd substituted tetrahedrite $Cu_{10}Cd_2Sb_4S_{13}$ microcrystals. At $T = 10$ K a single broad, asymmetric and structureless PL band was detected at about 1.08 eV. The temperature and laser power dependencies indicate that the properties of PL emission can be explained by the distant donor–acceptor (DA) pair model, where a donor defect has a depth of $E_D \approx 30$ meV and an acceptor defect $E_A = 88 \pm 6$ meV. It was shown that the shape of the DA pair band could be effectively described using statistical distribution of donor–acceptor defects, recombination probability of DA pairs with different spatial separation, relatively strong electron–phonon coupling and occupation probabilities of donor and acceptor defects. At $T = 200$ K the DA pair recombination gradually starts to transform into conduction band-acceptor recombination.

Keywords: donor–acceptor pairs, photoluminescence, tetrahedrite, absorber

(Some figures may appear in colour only in the online journal)

1. Introduction

The theoretical concept of donor–acceptor (DA) pair recombination in semiconductors was developed almost 60 years ago [1–5]. Since then DA pairs were systematically studied in different compound semiconductors like GaP, GaN, CdS and others. Most of these studies concentrate on narrow discrete photoluminescence (PL) peaks appearing at very low temperatures and being related to different lattice distances between donor and acceptor defects. At the same time, much less effort has been dedicated to the studies of distant or unassociated DA pairs, where the distribution of DA distances is more or less determined by statistics. These DA pairs usually give broad structureless PL bands. The full width at half maximum (FWHM) of these wide bands even at very low temperatures exceeds 0.2–0.3 eV. The first studies of these bands were made on binary compounds. Later DA bands were found also in ternary and multinary compounds like chalcopyrites, perovskites and kesterites [6–15]. However, multinary compounds usually have a very high concentration of charged intrinsic defects and as a result, conduction and valence band edges are often affected by the electrostatic potential fluctuations. The depth of these fluctuations can be bigger than the depth of shallow defect levels and therefore the traditional DA pair emission will be transformed into recombination through band tails [16, 17]. Obviously, distant DA pairs can be studied only in samples with very small depth of potential fluctuations, where shallow defect levels are not overlapped by band tails. Such compounds are also promising materials for optoelectronic applications like solar cells.

Recent years have shown that tetrahedrite copper antimony sulphide $Cu_{12}Sb_4S_{13}$ is a much stronger absorber than conventional solar absorbers such as kesterites, CdTe and $CuInSe_2$ [18, 19]. The bandgap energy of $Cu_{12}Sb_4S_{13}$ is around 1.7 eV [19, 20] but it offers different possibilities to tune the bandgap energy by cation substitution. It was first

shown that the bandgap energy of $Cu_{10}Zn_2Sb_4S_{13}$ is around 1.4 eV [18]. Therefore, cation substituted tetrahedrites could be quite attractive for photovoltaics and other applications. Tetrahedrites are also economically feasible thermoelectric materials, suitable for commercialization [18, 20–23]. The pure synthetic $Cu_{12}Sb_4S_{13}$ has a metallic behavior due to the mixed oxidation-state of Cu in its composition required for charge neutrality, i.e. 10 of the 12 Cu atoms are monovalent, while the remaining two Cu atoms are divalent. A mixture of formal oxidation states of Cu^{2+} (with d^9 configuration) and Cu^{1+} (with d^{10} configuration) results in the partly unfilled valence band with a high hole concentration giving rise to the high electrical p-type conductivity. Substitution of Cu^{2+} by Cd^{2+} (d^{10}) or by some other two-valent d^{10} element (Zn^{2+}, Ni^{2+}, etc) reduces the high carrier concentration and resistivity values as high as $\rho = 12.0\ \Omega$ cm can be reached [21]. Theoretical calculations predict solar cell efficiency values higher than for example CdTe solar cells [18]. Recently a first solar cell was demonstrated in tetrahedrite based material by partly substituting Cu with Cd ($Cu_{10}Cd_2Sb_4S_{13}$) [24]. However, optoelectronic properties of this material are not studied in detail so far and therefore more studies are needed to reveal the true potential of this material as a solar cell absorber. In this paper we present a first study of DA pair PL in tetrahedrite $Cu_{10}Cd_2Sb_4S_{13}$ (TH–Cd) microcrystals and show, that this material does not have potential fluctuations.

2. Experimental section

TH–Cd microcrystals used in this study were synthesized by the molten salt (flux material) synthesis-growth method [24]. Elemental Cu (Alfa Aesar, 5N), Sb (Alfa Aesar, 5N), S (5N) and binary CdS (5N) powders were used as precursors for the synthesis of $Cu_{10}Cd_2Sb_4S_{13}$ in molten CdI_2 (ACROS Organics, 2N) as a flux material. The precursors in the molar ratio of elements (Cu:Cd:Sb:S = 10:2:4:13) and the flux salt in the mass ratio of TH–Cd/CdI_2 = 1:1 (g/g) were mixed by grinding in an agate mortar. The mixture was loaded into a quartz ampoule, sealed under vacuum and annealed isothermally at 480 °C for 336 h. The synthesis–growth process was stopped by taking the ampoule out of furnace and cooling down to room temperature in air. After the opening of the ampoule the salt was removed from the formed solid microcrystal powder by leaching and rinsing with deionized H_2O. The powder was dried in a thermostat at 50 °C. The average size of obtained microcrystals was about 30 μm. More details about the growth process of $Cu_{10}Cd_2Sb_4S_{13}$ microcrystals can be found in [24]. The elemental and phase composition of the synthesized material were determined by energy dispersive x-ray spectroscopy (EDX) and Raman spectroscopy. The EDX analysis was performed on Zeiss Merlin high-resolution scanning electron microscope equipped with the Bruker Esprit 1.8 system (the measurement error is about 0.5 at.%). According to the EDX analysis, the TH–Cd crystals had an average composition of $Cu_{9.9}Cd_2Sb_{4.1}S_{13}$ i.e. it was very close to the stoichiometry.

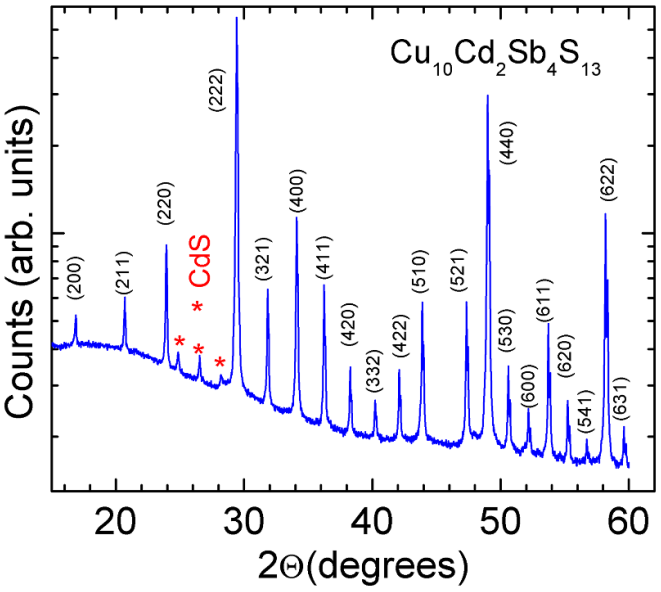

Figure 1. XRD pattern of studied $Cu_{10}Cd_2Sb_4S_{13}$ microcrystals in a logarithmic scale.

The crystal structure of the studied TH–Cd microcrystals was determined by x-ray diffraction (XRD) using a Rigaku Ultima IV diffractometer with monochromatic Cu Kα1 radiation ($\lambda = 1.5406$ Å) at 40 kV and 40 mA operating with the silicon strip detector D/teX Ultra. XRD analysis showed cubic crystal structure of tetrahedrite $Cu_{10}Cd_2Sb_4S_{13}$ phase with the space group *I-43 m* (ICDD PDF-2-2013, 00-062-0642). The lattice constants were determined using the Rietveld refinement procedure by Rigaku PDXL version 1.4.0.3 software. The lattice constant was $a = 10.507$ Å. Only a small portion (less than 1%) of the CdS phase was found as separate crystals. The XRD pattern is presented in figure 1 using a logarithmic scale in order to reveal weak CdS peaks.

Raman measurements were carried out using a Horiba LabRAM HR800 Micro-Raman system equipped with a cooled multichannel charge couple devive (CCD) detection system in the backscattering configuration with a spectral resolution better than 1 cm^{-1}. An He–Ne laser (wavelength $\lambda = 633$ nm) was used for excitation. The laser spot size was about 5 μm in diameter. Figure 2(a) presents a deconvoluted Raman spectrum of TH–Cd microcrystals fitted using Lorentzian functions to resolve the peaks. Fitting of the spectrum of $Cu_{10}Cd_2Sb_4S_{13}$ reveals several modes of vibration, the most intensive peaks in the spectra are observed at 110 and 363 cm^{-1}. The additional characteristic Raman modes are detected at 93, 245, 291, 327 and 353 cm^{-1} (see figure 2(a)). Assignment of the Raman peaks at 93, 110, 291, 327, 353 and 363 cm^{-1} characteristic to the Cd substituted tetrahedrite are presented in the previous work [24]. Very weak and broad bands at 80, 132, 173 and 245 cm^{-1} could also belong to the tetrahedrite phase.

A 0.64 m focal length single grating (600 mm^{-1}) monochromator and the 442 nm line of a He–Cd laser with different power were used for the PL measurements. For the PL signal detection a Hamamatsu InGaAs photomultiplier tube

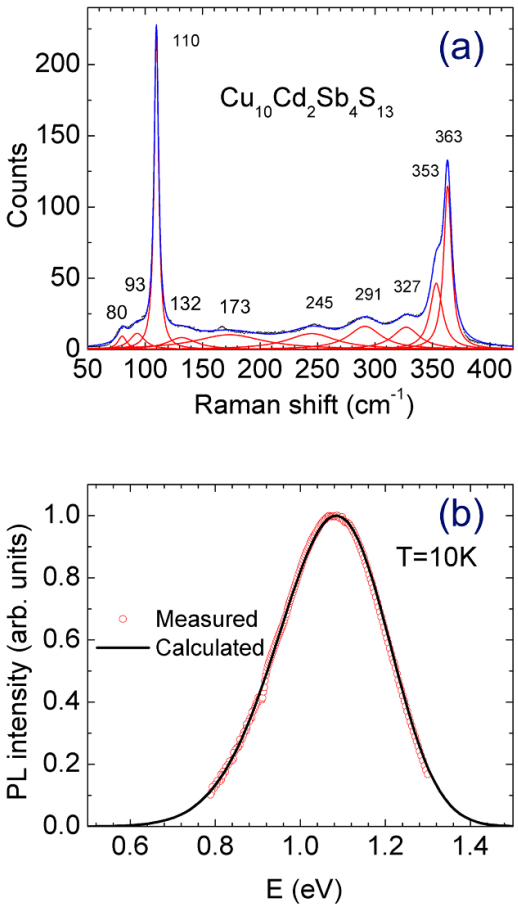

Figure 2. (a) Raman spectra of $Cu_{10}Cd_2Sb_4S_{13}$ tetrahedrite microcrystals. Result of fitting with Lorentzian curves is shown as solid lines. Laser excitation wavelength: $\lambda = 633$ nm. (b) Comparison of measured and calculated PL spectrum using equation (8) at $T = 10$ K.

(PMT) was used. A closed-cycle helium cryostat (Janis CCS-150) was employed to measure temperature dependencies of the PL spectra at temperatures from 10 K to 300 K.

3. Results and discussion

Measured PL spectra of $Cu_{10}Cd_2Sb_4S_{13}$ at different temperatures are enclosed in figure 3(a). The observed wide PL band has a slightly asymmetric shape and therefore the split pseudo-Voight function was used to fit all spectra.

It is known that the asymmetric shape at low temperatures can be caused by a strong electron–phonon coupling where phonon replicas follow a Poisson distribution or by the presence of exponential band tails in heavily doped materials, where the main recombination is related to these tails [16, 25–27]. As a rule, the low energy side of these asymmetric PL bands at low temperatures is then more or less determined by the density of states function $\rho(E)$ while the Fermi distribution function $f(E)$ controls the shape of the high energy side of the PL band [28].

The temperature dependence of the spectral energy of the PL intensity maxima E_{max}(T) for the observed band is presented in figure 3(b). It can be seen that with rising temperature the band shifts about 10 meV to lower energy until at $T \approx 200$ K, from where the PL band maxima starts to shift to higher energy. This behavior of E_{max}(T) is characteristic also for heavily doped materials, where carrier redistribution between potential wells is happening with increasing temperature [17, 26]. Therefore, the amount of red-shift in these materials is determined by the average depth of potential fluctuations γ and it is usually in the range of 30–50 meV. Moreover, in heavily doped materials the red-shift of the PL band is followed by the blue-shift and the amount of this blue-shift is normally less than the amount of red-shift [16, 26]. In our case at $T = 300$ K the peak position of the PL band is even at higher energy than at $T = 10$ K. This is rather unusual behavior for heavily doped materials whereas blue-shift of about 30 meV is typical for DA pair recombination, when at certain temperature donor levels will be ionized and the DA pair recombination transforms into the conduction band-acceptor (c–A) recombination [8, 29]. The maximum shift can be considered as an approximate depth of the donor level. The observed red-shift at low temperatures is then related to the ionization of donor levels of closest pairs (higher E_{max}) followed by the capture of released electrons by donor levels of more distant pairs (lower E_{max}). This kind of redistribution of electrons preserves the PL intensity and we do not observe noticeable thermal quenching at low temperature region.

Next, analysis of the temperature quenching of the PL band was carried out, see figure 3(a). An Arrhenius plot of the resulting integral intensity was fitted using a model of a single recombination channel and assuming the temperature dependence of the hole capture cross section proposed in [30]:

$$\Phi(T) = \Phi_0 / \left[1 + \alpha_1 T^{3/2} + \alpha_2 T^{3/2} \exp(-E_a/kT)\right], \quad (1)$$

where Φ_0 is the integral intensity of the PL band at 0 K, α_1 and α_2 are process rate parameters and E_a is the activation energy. The high temperature quenching is related to the ionization of the acceptor level with an activation energy of $E_a = 88 \pm 6$ meV and represents thus the depth of the acceptor defect level E_A. There is no visible drop of PL intensity at lower temperatures, where the ionization of more shallow donor levels starts and this is an indication that the recombination rates of DA pairs and c–A are quite similar.

Further analysis of the spectra reveals that a phonon broadening of the PL band also takes place when temperature increases. The traditional method for analysis of electron–phonon interaction in the case of PL bands with relatively large half-widths and without phonon structure is to compare the experimentally measured temperature dependence of the luminescence full width at half maximum FWHM(T) with the theoretical one, expressed as [31, 32]:

$$\mathrm{FWHM}(T) = \mathrm{FWHM}_0 \sqrt{coth\left(\frac{E_{ph}}{2kT}\right)}, \quad (2)$$

where FWHM_0 is the full half-width at 0 K, E_{ph} is the interacting 'effective' phonon energy in the excited state of the luminescence center. Although the equation (2) is an approximation,

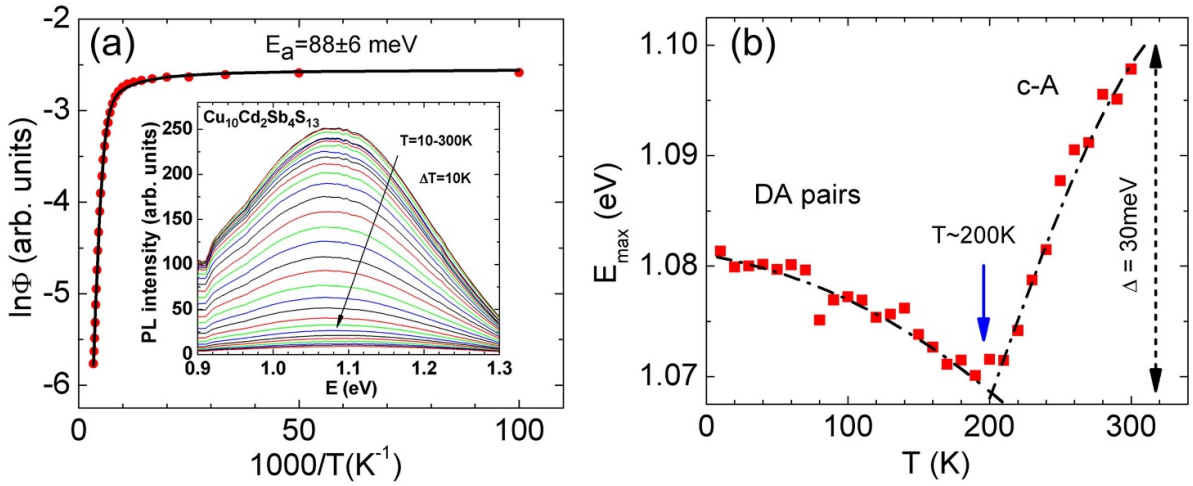

Figure 3. Temperature dependence of $Cu_{10}Cd_2Sb_4S_{13}$ PL band. (a) Integral intensity Φ. Solid curve shows the fitting result using equation (1). Insert displays PL spectra. (b) Temperature dependence of the PL peak position. The dash-dotted lines in the figure are guides for the eye.

especially the use of only one single 'effective' phonon instead of entire phonon spectrum, it often fits experimental data quite well in many semiconductor compounds [27, 32–35]. The result of this analysis is given in figure 4(a). According to the fitting with equation (2) the 'effective' phonon energy is $E_{ph} = 51$ meV (411 cm^{-1}). This energy is slightly higher than phonon modes detected by Raman spectroscopy, see figure 2(a). We can also notice a different behavior of half-width at half maximum (HWHM) values, see figure 4(a). At temperatures $T = 10$–180 K the $HWHM_L$ value (corresponding to the low-energy side of the PL band) shows only a very small rise with temperature while the $HWHM_H$ (high-energy side of the PL band) value constantly increases.

As a result, the PL band becomes almost symmetrical at temperatures $T > 200$ K. This behavior (at least at temperatures $T < 200$ K) is an indication that the PL band broadening with temperature is not caused by the electron–phonon interaction only but has more complex origin.

The dependence of the spectral position and integral intensity of the PL band at $T = 10$ K on the excitation power are shown in figure 4(b). Increasing laser power induces a small blue-shift (j-shift) of the spectral position of the PL band—about 6 meV per decade of laser power. The j-shift value less than 10 meV is typical for DA pair recombination [9, 36, 37] and is related to the saturation of recombination of more distant pairs. The actual blue-shift value usually depends on the DA pair distribution function and in the case of narrow distribution the blue-shift can be smaller than 3 meV per decade. In heavily doped materials a similar blue-shift is very common, but the rate of j-shift is always close to or higher than 10 meV per decade [25, 38, 39]. The dependence of the integral intensity Φ of the PL band on excitation laser power I can be described as $\Phi \sim I^m$, where m is a coefficient which can be determined from the gradient of a straight line fitted to a $\log(\Phi) - \log(I)$ scale, see figure 4(b). According to [40], the presence of defect energy levels within the bandgap results in the involvement of these defects in radiative recombination processes reducing m-values below unity whereas m values greater than unity should be taken as an indication of transitions not involving defects. Our experimental value of $m = 0.92$ is an additional proof, that in $Cu_{10}Cd_2Sb_4S_{13}$ the radiative recombination involves defect levels.

Let us look at the DA distant pair model in more detail. It is known that the PL peak energy for every single DA pair recombination is expressed as:

$$E_i(r) = E_g - (E_D + E_A) + \frac{e^2}{\varepsilon r_i}, \tag{3}$$

where E_g, E_D, and E_A are the band gap energy, and the donor and acceptor ionization energies, respectively, r_i is the distance between the donor and acceptor defects, and ε is the static dielectric constant [2, 3]. In the case of quite shallow donor and acceptor levels, when the carrier's wave functions spread over several lattice constants, the random statistical distribution of DA pairs $G(r)$ is given by:

$$G(r) = 4\pi r^2 N \exp\left(-\frac{4\pi r^3}{3}\right), \tag{4}$$

where N is a number of DA pairs [3]. Moreover, it is also known [1, 41] that the recombination probability of a DA pair W depends on distance r_i as:

$$W(r_i) = W_0 \exp\left(\frac{2r_i}{a_0}\right), \tag{5}$$

where a_0 is the sum of electron and hole Bohr radii. By combining equations (3)–(5) it is possible to convert the distribution function G of DA pairs and the recombination probability W to the energy scale: $G(E)$ and $W(E)$.

For closest DA pairs (highest E_{max}) the energy levels will be very close to the conduction and valence band edges and

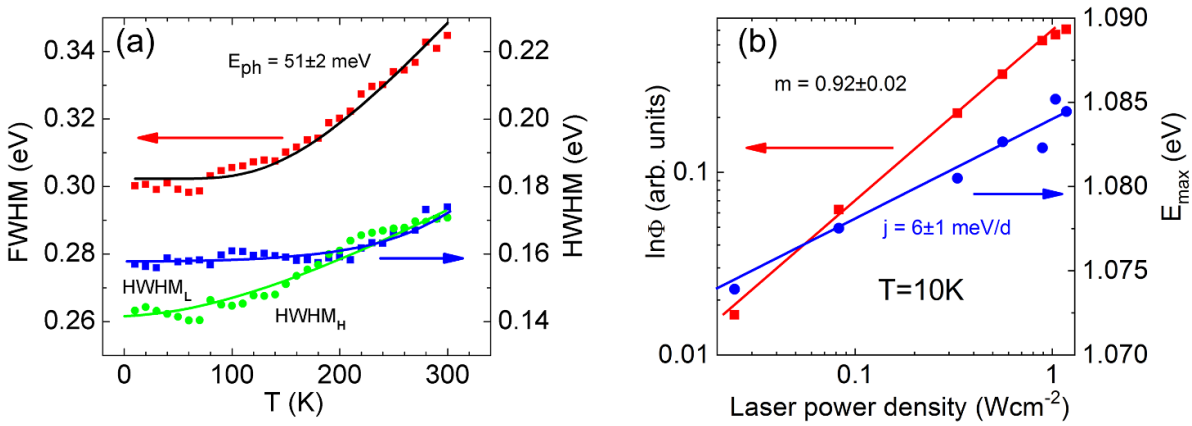

Figure 4. (a) Temperature dependence of the FWHM and HWHM's of the PL band. Black solid curve is a result of fitting using equation (2). The colored lines for HWHM's in the figure are guide for the eye. (b) Dependence of integral intensity Φ and peak position E_{max} on excitation intensity. Results of the fitting are presented as solid lines.

the occupation probability f of these levels is determined by the position of quasi-Fermi level E_f^*:

$$f(E) = \frac{1}{1 + \exp\left(E - E_f^*/kT^*\right)}. \quad (6)$$

We must also consider the temperature dependence of E_f^*

$$E_f^* = E_{g0} - kT^* \ln\left(\frac{n}{n_i}\right). \quad (7)$$

Here E_{g0} is a certain energy used in our model, n is a carrier concentration and n_i is an initial intrinsic carrier concentration and T^* is a carrier temperature. The energy scale was chosen according to our experimental PL spectra. In our model the increase of temperature moves the quasi-Fermi level closer to the peak position of the distribution, i.e. the high-energy side of the distribution will be affected. The product of $G(E_i)^* W(E_i)^* f(E_i)$ gives us the PL intensity of a single DA pair with emission energy E_i, see figure 5(a). However, the actual shape of the PL band with energy E_i is more or less determined by the electron–phonon interaction with optical and acoustic phonons. The electron–phonon coupling is often theoretically explained by using the configuration coordinate or Franck–Condon model, see for example [42, 43]. According to a conventional Franck–Condon model the absorption and emission spectrum are composed of a series of transitions separated by the phonon energy E_{ph}. The intensity of each transition is proportional to the overlap of the harmonic oscillator states in the ground and excited states of the DA pair. At low temperature only the ground vibrational state is occupied and the intensity of each transition is proportional to: $I(m) \sim \exp(-S)\, S^m/m!$ [42]. We can see that the spectral shape of a single DA pair emission is determined by a Poisson distribution of Gaussian peaks, shifted by the phonon energy E_{ph} (usually the longitudinal optical (LO)-phonon energy) and having the halfwidth w. This width is related to the electron–phonon interactions with low energy acoustic phonons. The distribution of LO-phonon replicas is then determined by the Huang–Rhys factor S, a dimensionless constant that gives the

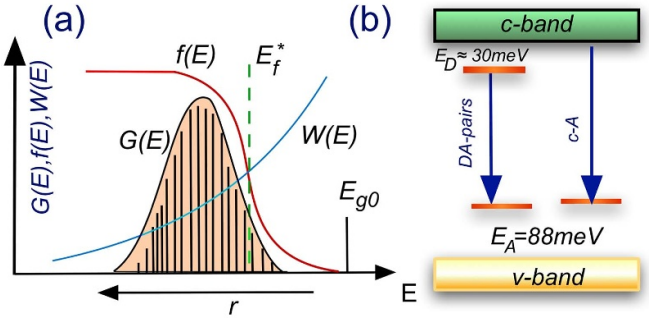

Figure 5. (a) Theoretical model of distributed DA pairs showing the contribution of various functions and describing the observed experimental PL spectra of $Cu_{10}Cd_2Sb_4S_{13}$ in this study. (b) Radiative recombination model in $Cu_{10}Cd_2Sb_4S_{13}$.

strength of the electron–phonon interaction. In the case of deep and wide PL bands the Huang–Rhys factor is usually in the range of $S \geqslant 3$ while for edge emission it could be less than 1 [25, 43]. In general, deeper defects show a stronger electron–phonon coupling and thus wider PL bands and higher Huang–Rhys factor. This is due to the fact that deep defects are more localized, and any change in their charge state thus leads to a significant lattice relaxation.

Then, in principle, it is possible to estimate the total shape of the PL band, where the contribution of all individual DA pairs is summarized:

$$I(E) = \sum_{i=1}^{N} G(E_i)\, W(E_i) f(E_i) \sum_{m=0}^{\infty} \frac{\exp(-S)\, S^m}{m!} \exp\left[\frac{-4\ln 2 (E_{0i} - mE_{ph} - E)^2}{w^2}\right], \quad (8)$$

where E_{ph} is a LO-photon energy, S is the Huang–Rhys factor, E_{0i} is the position of zero-phonon line for i-DA pair, and w is a Gaussian broadening of the transitions.

We neglected the temperature dependence of w, because at low temperatures it is usually constant or has only a very

weak increase. The result of calculations using equation (8) for $T = 10$ K is shown in figure 2(b) as a solid line.

Numerical simulations with equation (8) revealed a few important features. At low temperatures the total PL band has an asymmetrical shape with a steeper decline at the high-energy side. This shape is mainly caused by the *f(E)* function. With the temperature increase the peak position of the PL band shows a certain red-shift while the low-energy side of the PL band does not show any changes. At the same time, constant broadening of the high-energy side of the PL band resulting in reduced asymmetry of the band is found. All these features are also observed experimentally. In order to match the experimental PL spectra with the theoretical ones, the half-width value of individual DA pair bands must be about 0.2 eV, even at very low temperatures. This value is possible when the Huang–Rhys factor S is between $S = 3$–4 and the LO-phonon energy is kept constant $\hbar\omega = 51$ meV. In this case, the highest energy zero-phonon peak E_0 can be found at 1.27 eV and the Franck–Condon shift between the PL peak position and the position of the zero-phonon line is in the range of 140–180 meV. Relatively strong electron phonon coupling is most probably related to the acceptor defect of DA-pairs. The low temperature bandgap energy can be estimated: $E_g = E_0 + E_A + E_D \approx 1.38$ eV. This E_g value is in a good correlation with the room temperature bandgap energy value $E_g = 1.3$ eV measured in our previous paper [24].

4. Conclusions

In conclusion, we present a recombination model for the TH–Cd microcrystals, see figure 5(b). At low temperatures, the DA pair recombination is dominating with $E_D \approx 30$ meV and $E_A = 88 \pm 6$ meV. At temperatures $T > 200$ K the DA pair recombination is gradually transformed into band-to-acceptor recombination. According to this model the bandgap energy E_g at low temperatures is about 1.38 eV. The suitable bandgap energy, absence of electrostatic potential fluctuations and relatively high absorption coefficient confirm that TH–Cd can be potentially appropriate absorber material for future thin film solar cells.

Acknowledgments

This work has been supported by the European Regional Development Fund, Project TK141. The authors would also like to thank Dr Mere for the XRD measurements. Grossberg is thankful to the L'Oréal Baltic For Women in Science Programme.

Conflict of interest

The authors declare no conflict of interest.

ORCID iDs

Jüri Krustok https://orcid.org/0000-0002-4671-2332
Taavi Raadik https://orcid.org/0000-0001-9831-665X
Reelika Kaupmees https://orcid.org/0000-0002-1766-4837
Fairouz Ghisani https://orcid.org/0000-0002-1232-7807
Kristi Timmo https://orcid.org/0000-0001-6054-6783
Mare Altosaar https://orcid.org/0000-0002-8815-3495
Maarja Grossberg https://orcid.org/0000-0003-3357-189X

References

[1] Thomas D G, Hopfield J J and Augustyniak W M 1965 Kinetics of radiative recombination at randomly distributed donors and acceptors *Phys. Rev.* **140** A202–20
[2] Thomas D G, Gershenzon M and Trumbore F A 1964 Pair spectra and 'edge' emission in gallium phosphide *Phys. Rev.* **133** A269–79
[3] Williams F 1968 Donor—acceptor pairs in semiconductors *Phys. Status Solidi* **25** 493–512
[4] Colbow K and Yuen K 1972 Radiative recombination in cadmium sulfide *Can. J. Phys.* **50** 1518–38
[5] Dingle R and Ilegems M 1971 Donor-acceptor pair recombination in GaN *Solid State Commun.* **9** 175–80
[6] Ozaki S, Boku S and Adachi S 2003 Optical absorption and photoluminescence in the defect-chalcopyrite-type semiconductor $ZnIn_2Te_4$ *Phys. Rev.* B **68** 235201
[7] Gasanly N M, Serpengüzel A, Aydinli A, Gürlü O and Yilmaz I 1999 Donor-acceptor pair recombination in $AgIn_5S_8$ single crystals *J. Appl. Phys.* **85** 3198–201
[8] Bai L, Giles N C, Schunemann P G, Pollak T M, Nagashio K and Feigelson R S 2004 Donor-acceptor pair emission near 0.55 eV in $CdGeAs_2$ *J. Appl. Phys.* **95** 4840–4
[9] Aihara N, Tanaka K, Uchiki H, Kanai A and Araki H 2015 Donor-acceptor pair recombination luminescence from monoclinic Cu_2SnS_3 thin film *Appl. Phys. Lett.* **107** 032101
[10] Krustok J, Raudoja J, Krunks M, Mändar H and Collan H 2000 Nature of the native deep localized defect recombination centers in the chalcopyrite and orthorhombic $AgInS_2$ *J. Appl. Phys.* **88** 205–9
[11] Hamanaka Y, Ogawa T, Tsuzuki M, Ozawa K and Kuzuya T 2013 Luminescence properties of chalcopyrite $AgInS_2$ nanocrystals: their origin and related electronic states *J. Lumin.* **133** 121–4
[12] Marceddu M, Anedda A, Carbonaro C M, Chiriu D, Corpino R and Ricci P C 2006 Donor–acceptor pairs and excitons recombinations in $AgGaS_2$ *Appl. Surf. Sci.* **253** 300–5
[13] Shirakata S, Chichibu S, Matsumoto S and Isomura S 1994 Zn-related donor-acceptor pair emission in $CuAlSe_2$ epitaxial layers *Japan. J. Appl. Phys.* **33** L345–7
[14] Luckert F *et al* 2011 Optical properties of high quality $Cu_2ZnSnSe_4$ thin films *Appl. Phys. Lett.* **99** 062104
[15] Kong W, Ye Z, Qi Z, Zhang B, Wang M, Rahimi-Iman A and Wu H 2015 Characterization of an abnormal photoluminescence behavior upon crystal-phase transition of perovskite $CH_3NH_3PbI_3$ *Phys. Chem. Chem. Phys.* **17** 16405–11
[16] Krustok J, Collan H, Yakushev M and Hjelt K 1999 The role of spatial potential fluctuations in the shape of the PL bands of multinary semiconductor compounds *Phys. Scr.* **T79** 179–82
[17] Krustok J, Raudoja J, Yakushev M, Pilkington R D D and Collan H 1999 On the shape of the close-to-band-edge photoluminescent emission spectrum in compensated $CuGaSe_2$ *Phys. Status Solidi* **173** 483–90
[18] Heo J, Ravichandran R, Reidy C F, Tate J, Wager J F and Keszler D A 2015 Design meets nature: tetrahedrite solar absorbers *Adv. Energy Mater.* **5** 1401506

[19] Rath T, MacLachlan A J, Brown M D and Haque S A 2015 Structural, optical and charge generation properties of chalcostibite and tetrahedrite copper antimony sulfide thin films prepared from metal xanthates *J. Mater. Chem.* A **3** 24155–62
[20] van Embden J, Latham K, Duffy N W and Tachibana Y 2013 Near-infrared absorbing $Cu1_2Sb_4S_{13}$ and Cu_3SbS_4 nanocrystals: synthesis, characterization, and photoelectrochemistry *J. Am. Chem. Soc.* **135** 11562–71
[21] Prem Kumar D S, Chetty R, Rogl P, Rogl G, Bauer E, Malar P and Mallik R C 2016 Thermoelectric properties of Cd doped tetrahedrite: $Cu_{12-x}Cd_xSb_4S_{13}$ *Intermetallics* **78** 21–29
[22] Tablero C 2014 Electronic and optical property analysis of the Cu–Sb–S tetrahedrites for high-efficiency absorption devices *J. Phys. Chem.* C **118** 15122–7
[23] Chetty R, Bali A and Mallik R C 2015 Tetrahedrites as thermoelectric materials: an overview *J. Mater. Chem.* C **3** 12364–78
[24] Ghisani F, Timmo K, Altosaar M, Raudoja J, Mikli V, Pilvet M, Kauk-Kuusik M and Grossberg M 2020 Synthesis and characterization of tetrahedrite $Cu_{10}Cd_2Sb_4S_{13}$ monograin material for photovoltaic application *Mater. Sci. Semicond. Process.* **110** 104973
[25] Spindler C, Babbe F, Wolter M H, Ehré F, Santhosh K, Hilgert P, Werner F and Siebentritt S 2019 Electronic defects in Cu(In,Ga)Se_2: towards a comprehensive model *Phys. Rev. Mater.* **3** 090302
[26] Levanyuk A P and Osipov V V 1981 Edge luminescence of direct-gap semiconductors *Sov. Phys. Usp.* **24** 187–215
[27] Krustok J, Valdna V, Hjelt K and Collan H 1996 Deep center luminescence in p-type CdTe *J. Appl. Phys.* **80** 1757–62
[28] Krustok J, Raadik T, Kaupmees R, Grossberg M, Kauk-Kuusik M, Timmo K and Mere A 2019 Observation of band gap fluctuations and carrier localization in $Cu_2CdGeSe_4$ *J. Phys. D: Appl. Phys.* **52** 285102
[29] Yakushev M V, Forbes I, Mudryi A V, Grossberg M, Krustok J, Beattie N S, Moynihan M, Rockett A and Martin R W 2015 Optical spectroscopy studies of $Cu_2ZnSnSe_4$ thin films *Thin Solid Films* **582** 154–7
[30] Krustok J, Collan H and Hjelt K 1997 Does the low-temperature Arrhenius plot of the photoluminescence intensity in CdTe point towards an erroneous activation energy? *J. Appl. Phys.* **81** 1442–5
[31] Keil T H 1965 Shapes of impurity absorption bands in solids *Phys. Rev.* **140** A601–17
[32] Ermolovich I B, Matvievskaja G I and Sheinkman M K 1975 Electron-phonon interactions at radiative carrier capture on deep centers in cadmium sulfide single crystals *J. Lumin.* **10** 58–68
[33] Williams E W 1968 Evidence for self-activated luminescence in GaAs: the gallium vacancy-donor center *Phys. Rev.* **168** 922–8
[34] Peak J D, Melcher C L and Rack P D 2011 Investigating the luminescence properties as a function of activator concentration in single crystal cerium doped Lu_2SiO_5: determination of the configuration coordinate model *J. Appl. Phys.* **110** 013511
[35] Krustok J, Mädasson J and Hiie J 1998 Photoluminescence properties of Z-bands in CdTe *Phys. Status Solidi* **165** 517–25
[36] Spindler C, Regesch D and Siebentritt S 2016 Revisiting radiative deep-level transitions in $CuGaSe_2$ by photoluminescence *Appl. Phys. Lett.* **109** 032105
[37] Shrestha N, Grice C R, Bastola E, Liyanage G K, Phillips A B, Heben M J, Yan Y and Ellingson R J 2018 Low temperature photoluminescence spectroscopy of defect and interband transitions in $CdSe_xTe_{1-x}$ thin films *MRS Adv.* **3** 3293–9
[38] Wagner M, Dirnstorfer I, Hofmann D M, Lampert M D, Karg F and Meyer B K 1998 Characterization of CuIn(Ga)Se_2 thin films: III. In-rich layers *Phys. Status Solidi* A **168** 163–75
[39] Yakushev M V, Jack A, Pettigrew I, Feofanov Y, Mudryi A V and Krustok J 2006 Low temperature air-annealing of Cu(InGa)Se_2 single crystals *Thin Solid Films* **511–2** 135–9
[40] Schmidt T, Lischka K and Zulehner W 1992 Excitation-power dependence of the near-band-edge photoluminescence of semiconductors *Phys. Rev.* B **45** 8989–94
[41] Colbow K 1965 Electrophotoluminescence in semiconductors *Phys. Rev.* **139** A274–84
[42] Huang K and Rhys A 1950 Theory of light absorption and non-radiative transitions in F-centres *Proc. R. Soc.* A **204** 406–23
[43] Alkauskas A, McCluskey M D and Van de Walle C G 2016 Tutorial: defects in semiconductors—combining experiment and theory *J. Appl. Phys.* **119** 181101